Cite This: ACS Appl. Mater. Interfaces 2018, 10, 9957–9968

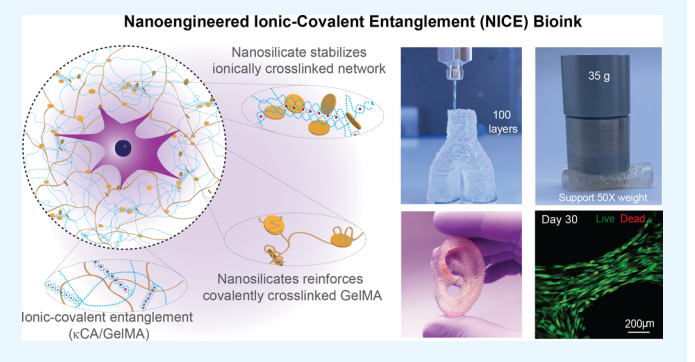
Nanoengineered Ionic-Covalent Entanglement (NICE) Bioinks for 3D **Bioprinting**

David Chimene, [†] Charles W. Peak, [†] James L. Gentry, [†] James K. Carrow, [†] Lauren M. Cross, [†] Eli Mondragon, [†] Guinea B. Cardoso, [†] Roland Kaunas, [†] and Akhilesh K. Gaharwar*, [†], [‡], [§] ©

[†]Department of Biomedical Engineering, [‡]Department of Materials Science and Engineering, and [§]Center for Remote Health and Technology, Texas A&M University, College Station, Texas 77843, United States

Supporting Information

ABSTRACT: We introduce an enhanced nanoengineered ionic-covalent entanglement (NICE) bioink for the fabrication of mechanically stiff and elastomeric 3D biostructures. NICE bioink formulations combine nanocomposite and ioniccovalent entanglement (ICE) strengthening mechanisms to print customizable cell-laden constructs for tissue engineering with high structural fidelity and mechanical stiffness. Nanocomposite and ICE strengthening mechanisms complement each other through synergistic interactions, improving mechanical strength, elasticity, toughness, and flow properties beyond the sum of the effects of either reinforcement technique alone. Herschel-Bulkley flow behavior shields



encapsulated cells from excessive shear stresses during extrusion. The encapsulated cells readily proliferate and maintain high cell viability over 120 days within the 3D-printed structure, which is vital for long-term tissue regeneration. A unique aspect of the NICE bioink is its ability to print much taller structures, with higher aspect ratios, than can be achieved with conventional bioinks without requiring secondary supports. We envision that NICE bioinks can be used to bioprint complex, large-scale, cell-laden constructs for tissue engineering with high structural fidelity and mechanical stiffness for applications in custom bioprinted scaffolds and tissue engineered implants.

KEYWORDS: bioinks, nanocomposites, bioprinting, ionic-covalent entanglement (ICE) network, hydrogels

INTRODUCTION

Three-dimensional (3D) bioprinting is emerging as a promising method for rapid fabrication of biomimetic cell-laden constructs for tissue engineering using cell-containing hydrogels, called bioinks, that can be cross-linked to form a hydrated matrix for encapsulated cells. 1-4 However, extrusion-based 3D bioprinting has hit a bottleneck in progress because of the lack of available bioinks with high printability, mechanical strength, and biocompatibility. 5,6 The printability of a bioink refers to the ability to print human-scale tissue and organ structures while smoothly extruding the intended architecture with high fidelity. Although recently developed bioinks enable precise deposition of viable cells, their printability in the Z-axis is hampered by limited structural integrity to support additional layers.⁶ Efforts to improve printability have largely focused on printing multiple materials into a single structure as well as functionalizing polymers for new cross-linking mechanisms.⁷⁻¹⁵ Other recent developments include novel strengthening mechanisms like interpenetrating networks, 16 self-healing hydrogels, 11,17 and nanocomposites. 18,19 Despite these efforts, existing bioinks remain severely limited when printing high aspect-ratio structures over 10 mm tall. These restricted vertical scales prevent replication of large scale 3D tissue organization and confines bioprinting applications to a

relatively flat plane. Some recent studies have circumvented this issue through complex thermoplastic support structures and suspension preparations.^{6,7} However, these techniques do not address the fundamental lack of bioinks with appropriate mechanical and bioresponsive properties.

To overcome the limitations of existing bioinks, we report the development of a highly printable bioink for fabricating large scale, cell-laden, bioactive scaffolds. These improvements are achieved through a novel bioink strengthening strategy that combines nanocomposite reinforcement 20,21 with ioniccovalent entanglement (ICE)²²⁻²⁴ to create a bioactive nanoengineered ionic-covalent entanglement (NICE) bioink with excellent printability, mechanical properties, and shape fidelity (Figure 1a). Nanocomposites and ICEs have been investigated separately for improving mechanical properties, but have never been applied simultaneously to a bioink for tissue engineering or bioprinting applications.

Received: December 29, 2017 Accepted: February 20, 2018 Published: February 20, 2018

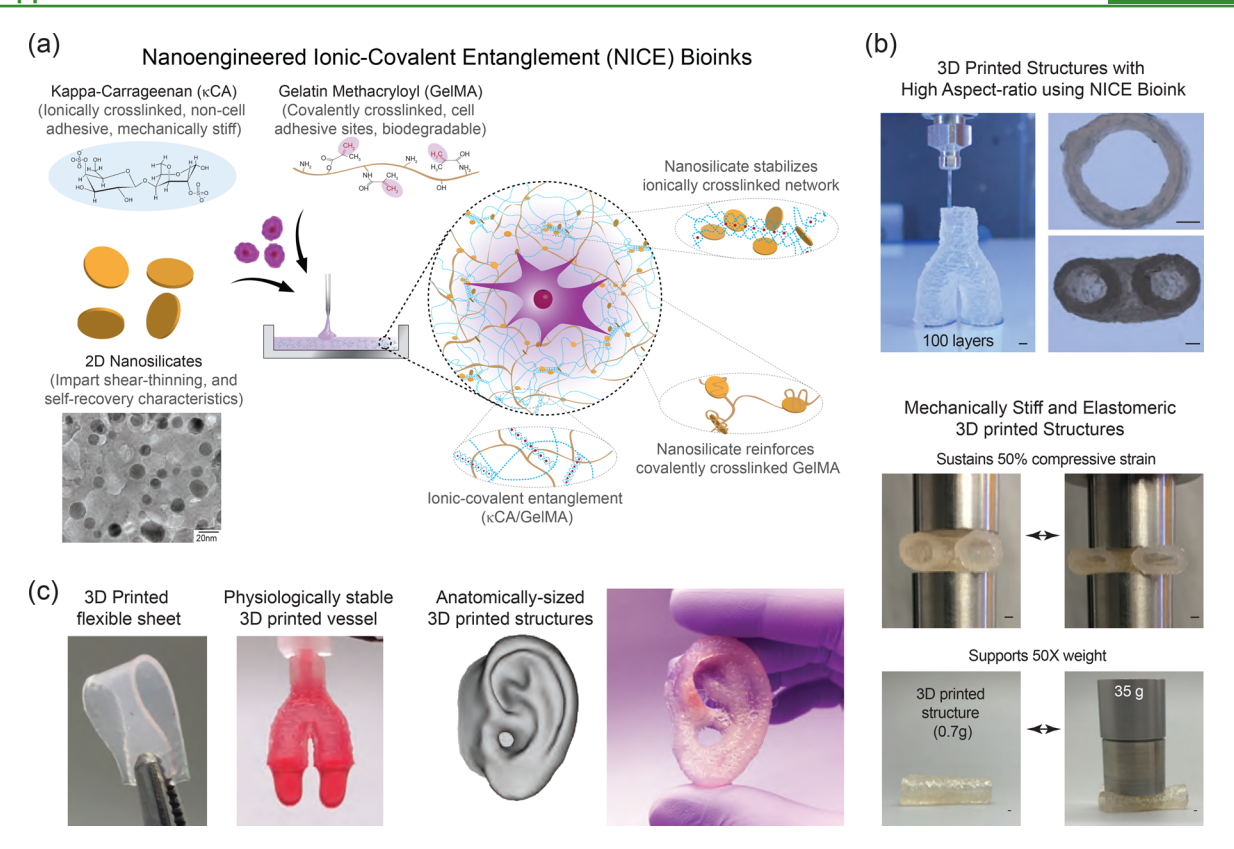


Figure 1. NICE bioinks combine nanocomposite reinforcement and ionic—covalent entanglement reinforcement mechanisms to create a bioink that is tough, elastic, and highly printable. (a) The NICE bioinks use nanosilicates to reinforce an ionic—covalent entanglement hydrogel made from GelMA and κ CA, creating a dually reinforced hydrogel network. These interactions allow the NICE bioink to behave as a solid at low shear stresses and improve shear thinning characteristics during bioprinting. After cross-linking, ICE and nanosilicate reinforcement synergistically improve mechanical strength. TEM imaging of two-dimensional nanosilicate particles showing uniform morphology. (b) The NICE bioinks print freestanding hydrogel structures with a high aspect-ratios and high print fidelity (scale bar = 1 mm). The cross-linked structures are stiff and elastomeric, and can support more than 50-times their own weight. (c) The 3D printed structures from NICE bioink are mechanically (film) and physiologically (bifurcated vessel) stable, and have high structural fidelity (3D printed ear).

■ RESULTS AND DISCUSSION

We demonstrate this technology by taking gelatin, a popular bioactive polymer that is poorly printable, and applying NICE reinforcement to engineer a printable and mechanically strong bioink. The low-cost, cell-adhesive, and enzymatically-degradable NICE bioink can print high aspect-ratio structures that are mechanically stiff and elastomeric (Figure 1b), including selfsupporting, anatomically sized structures (Figure 1c). The NICE bioink was evaluated against individual component polymers and strengthening mechanisms (nanocomposites and ICEs) to establish their contributions to NICE bioink properties. Our results demonstrate that combining nanocomposite and ICE reinforcement synergistically enhances the printability and mechanical properties without compromising bioactivity, making NICE bioinks well-suited for bioprinting larger, more complex tissue structures than were possible with previous bioinks.

ICE networks are composed of two entangled, yet independent polymer networks cross-linked only to themselves through the use of distinct cross-linking mechanisms.²⁵ This recently developed hydrogel strengthening process is fast and cytocompatible, unlike conventional dual-network strategies, making it well-suited for incorporation into the 3D bioprinting toolkit. The increase in strength and toughness from ICE reinforcement is attributed to stress-sharing between networks to reduce stress concentrations, as well as energy dissipation

through reversible disruption of ionic network cross-links while the more flexible covalently cross-linked network remains intact. This mechanism also allows ICE networks to exhibit elastomeric characteristics under mechanical loading without compromising mechanical strength. ^{22–24}

To create a suitable ICE bioink, we combined bioactive gelatin methacryloyl (GelMA) with kappa-carrageenan (κCA). GelMA is obtained by partially hydrolyzing collagen to improve solubility, and subsequently functionalizing to allow covalent cross-linking under ultraviolet (UV) light. GelMA hydrogels retain many essential properties of native extracellular matrix, including cell attachment sites and matrix metalloproteinase (MMP) motifs that allow cells to remodel the hydrogel network. GelMA also undergoes thermally sensitive physical gelation around 30 °C, helping to stabilize bioprinted structures. CA is a linear polysaccharide commonly used in foods, pharmaceuticals, and cosmetics, and was chosen as the ionic cross-linking ICE polymer for its solubility, biocompatibility, and track record of successful use in previous ICE hydrogel experiments.

The GelMA/ κ CA ICE network was reinforced by incorporating two-dimensional (2D) Laponite XLG nanosilicates (nSi). These nanosilicates are disc-shaped, mineral nanoparticles 30–50 nm in diameter and \sim 1 nm in thickness. Negatively charged faces and positively charged edges allow reversible electrostatic interactions with the charged polymer backbones. Nanosilicate interactions can improve stiffness, elasticity, adhesiveness,

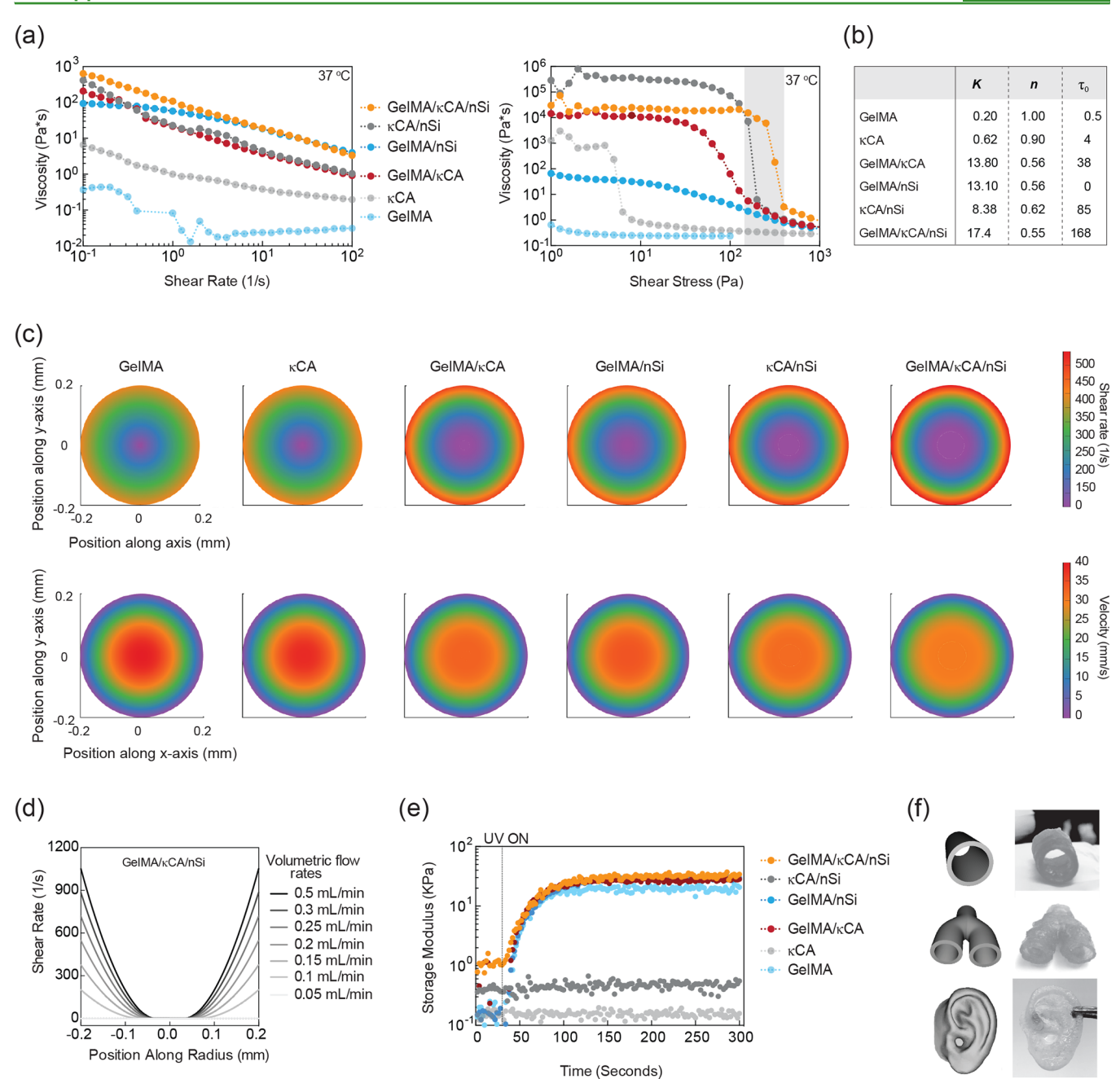


Figure 2. Rheological characterization of the NICE bioink. (a) The shear stress sweeps measure viscosity changes with increasing shear stress, allowing visual comparison of the yield regions of each bioink (NICE yield region shaded on graph). Shear rate sweeps illustrate the shear thinning characteristics of pre-crosslinked gels. (b) The rheological characteristics of precross-linked gels derived by fitting shear stress sweep to the Herschel-Bulkley (HB) model. HB model characteristics include K (consistency index), n (power law index), and τ_0 (yield stress). (c) The yield region data is fit to a Herschel-Bulkley Fluid model, allowing bioink flow through the extruder tip to be simulated under experimental conditions (0.15 mL/min, 20 mm/s at 37 °C) as they pass through the extruder tip. (d) The 2D profiles of the NICE bioink shear rate profile at different flow rates during extrusion printing. Flow rates from 0.05 to 0.5 mL/min are graphed, including our experimental bioink. (e) UV rheology shows formation of covalently cross-linked network due to presence of GelMA when exposed to UV light (25 mW/cm²). (f) The NICE bioink can be used to print human-scale relevant 3D printed structures (cylindrical, Y-shaped blood vessel, and ear). These three anatomical models highlight the high print fidelity between models and the printed structures.

viscoelastic modulus, and cell adhesion in some hydrogels, and imbue hydrogel solutions with complex fluid behavior that can improve bioprintability.^{32–34} Furthermore, Laponite nanosilicates have shown broad biocompatibility in vivo and in vitro, and are used extensively in cosmetics and toothpastes as well as in drug delivery and tissue engineering.^{33,35,36} Previous studies have demonstrated that polyampholytic gelatin chains are strongly attracted to the negatively charged faces of

nanosilicates, while κ CA preferentially interacts with the positively charged edges of nanosilicates. Dynamic light scattering and zeta potential experiments confirm that both GelMA and κ CA interact strongly with nSi (Figure S1) as shown by the increase in hydrodynamic diameter and stabilization of zeta potential. In the NICE bioink, we hypothesize that 2D nanosilicates form reversible bonds with both GelMA and κ CA, acting as a secondary electrostatic cross-

linking mechanism to improve the viscoelastic properties and printability of the bioink. 37

NICE Reinforcement Improves Printability of Precross-linked Bioink. Effective 3D bioprinting requires bioinks to exhibit complex fluid behaviors, but these requirements remain poorly defined despite the rapid expansion of this field. With this in mind, we examined the rheological characteristics of our bioinks (prior to cross-linking), including shear thinning behavior (shear rate sweep) and yield point (shear stress sweep, amplitude stress sweep) at room (25 °C) and physiological (37 °C) temperatures, compared with individual component gels (Figure 2a, b and Figure S2). Shear rate sweep results indicate that all formulations except GelMA display clear shear-thinning behavior in that an increase in shear rate or shear stress results in a decrease in viscosity. GelMA's gelation temperature is below physiological temperature, causing it to exhibit low viscosity fluid-like behavior (<1 Pa s) at 37 °C for all shear rates and shear stresses. The addition of nanosilicates increases the viscosities of GelMA and κCA alone and of GelMA/κCA combined.

The shear stress sweep was performed over a range of shear magnitudes where the polymer viscosity transitions from a solid-like to liquid-like state (i.e., yield stress). This behavior can be described by the Herschel-Bulkley fluid model, $\tau = \tau_0 +$ $K(\dot{\gamma})^n$, where τ and τ_0 represent apparent and yield stress, respectively, and $\dot{\gamma}$ is the shear rate. The consistency index (K), is the apparent viscosity of the fluid at a shear rate of 1 s^{-1} . The power law index, n, expresses how non-Newtonian a fluid is: when n = 1, the fluid is considered Newtonian, whereas n < 1and n > 1 indicate shear thinning and thickening, respectively. The tabulated results show that all formulations exhibited shear-thinning behavior at 37 °C except GelMA (n = 1.00). The addition of nanosilicates reduced the power law index of GelMA (1.00 \rightarrow 0.56) and κ CA (0.90 \rightarrow 0.62). Mixing GelMA and κ CA also resulted in a low power law index that was only slightly influenced by addition of nanosilicates (0.56 \rightarrow 0.55), most likely because the baseline value was already low. These reductions confirm that adding nanosilicates and KCA increases shear thinning, which improves printability by reducing flow resistance at the high shear rates generated during extrusion. Similarly, the addition of nanosilicates increased the consistency index (K) of GelMA (K: $0.2 \rightarrow 13.1$) and increased both K and τ_0 of κ CA (K: 0.62 \rightarrow 8.38, τ_0 : 4 \rightarrow 85 Pa). Mixing GelMA with κ CA also increased the consistency index and yield stress and this was further increased by addition of nanosilicates (K: 13.8 \rightarrow 17.4, τ_0 : 38 \rightarrow 168 Pa). Higher yield stresses allow bioprinted structures to behave as a viscoelastic solid even before covalent cross-linking, preventing layer spreading after extrusion and increasing print fidelity. These results suggest that ionic-covalent entanglement and electrostatic interactions between nanosilicate and polymer chains synergistically reinforce NICE bioinks.

In addition to improving print fidelity, viscosity and high yield stress combined with shear thinning characteristics also serves to shield cells from damaging shear stresses during extrusion. ^{38–40} The Herschel-Bulkley fluid model parameters were used to predict shear rate and velocity distributions for fully developed flow within the extrusion tip during bioprinting (Figure 2c and Figure S3). In these models, the shear rate and velocity profiles of the different inks were simulated under our experimental conditions (0.15 mL/min, 20 mm/s at 37 °C) as they pass through the extruder tip.

Individual polymer components (GelMA and κ CA) exhibited low shear thinning and yield stress when subjected to a constant flow rate to mimic extrusion bioprinting. The addition of nanosilicates increases the size of the plug-flow region for all formulations, with NICE bioinks having the greatest area experiencing plug flow. Plug flow shields encapsulated cells from damaging shear stress and extrudes the bioink as a viscoelastic solid ($\tau < \tau_0$), thereby increasing print fidelity.^{38–40} To further investigate the ability of NICE bioink for bioprinting, we determined the flow profile through a 400 μ m cannula at extrusion rates between 0.05 and 0.5 mL/min, resulting in that plug flow occurring at all extrusion rates (Figure 2d). A flow rate of 0.15 mL/min (print speed 20 mm/ s) was selected for all experiments for rapid bioprinting. Overall, this simulation suggests that nanosilicates and κ CA synergistically improve shear-thinning and yield stress in the NICE bioink, causing the NICE bioink to exhibit cell-shielding plug flow that allows the bioink to be extruded as viscoelastic solids at the optimized print parameters. The maximum predicted shear stresses (Figure S4) were well within the safe range for bioprinted cells, 4,41 suggesting that even higher extrusion rate bioprinting is safe with the NICE bioink.

After printing was complete, 3D-printed structures were dual-cross-linked with UV light (25 mW/cm² at 365 nm) and 5% KCl to obtain mechanically stable structures. The covalently cross-linked GelMA network is formed within 60–80 s. To quantify the gelation kinetics, a time sweep was performed by monitoring storage modulus of bioink formulations in the presence of UV light (Figure 2f and Figure S5). All bioink formulations containing photo-cross-linkable GelMA (GelMA, GelMA/nSi, GelMA/κCA, and GelMA/κCA/nSi) rapidly solidified under exposure to UV light. The inclusion of κCA and nanosilicates did not significantly affect the rate of UV gelation.

We next evaluated the printability of the NICE bioink by printing physiologically relevant structures (Figure 2e). As previously mentioned, printability refers to the ability to print high aspect-ratio structures at human-relevant scales, and extrude the intended structure smoothly and with high fidelity. Conventional bioinks print precisely on the x- and y-axes but collapse under the weight of subsequent layers, causing 3D structures to have poor print fidelity, particularly along the z-axis(height). Therefore, our bioinks were tested on all 3 axes to objectively quantify printability.

We attempted to print the simplest possible structure that meets these requirements using each bioink: a hollow cylinder approximating the shape of a human-scale bronchus or blood vessel. The shape used for printability quantification was an 8 mm interior diameter cylinder with 1 mm thick walls, and when using the NICE bioink, a stable structure was printed up to 3 cm (150 layers) in height (Figure S6). In contrast, none of the component inks (GelMA, GelMA/nSi, κCA, κCA/nSi, GelMA/ κ CA) could print cylinders above 3 mm (15 layers) without collapse. Layer spreading was quantified by measuring the cylinder wall thickness of the lowest 5 and highest 5 layers, revealing that wall thickness measurements of NICE cylinders remained within ±10% of intended diameter at all measured points. Shape fidelity was measured by comparing the actual height and diameter of the printed cylinder to its intended ideal dimensions, which revealed no significant variations in either

More complex structures were also bioprinted to demonstrate the range of the NICE bioink's potential applications. A

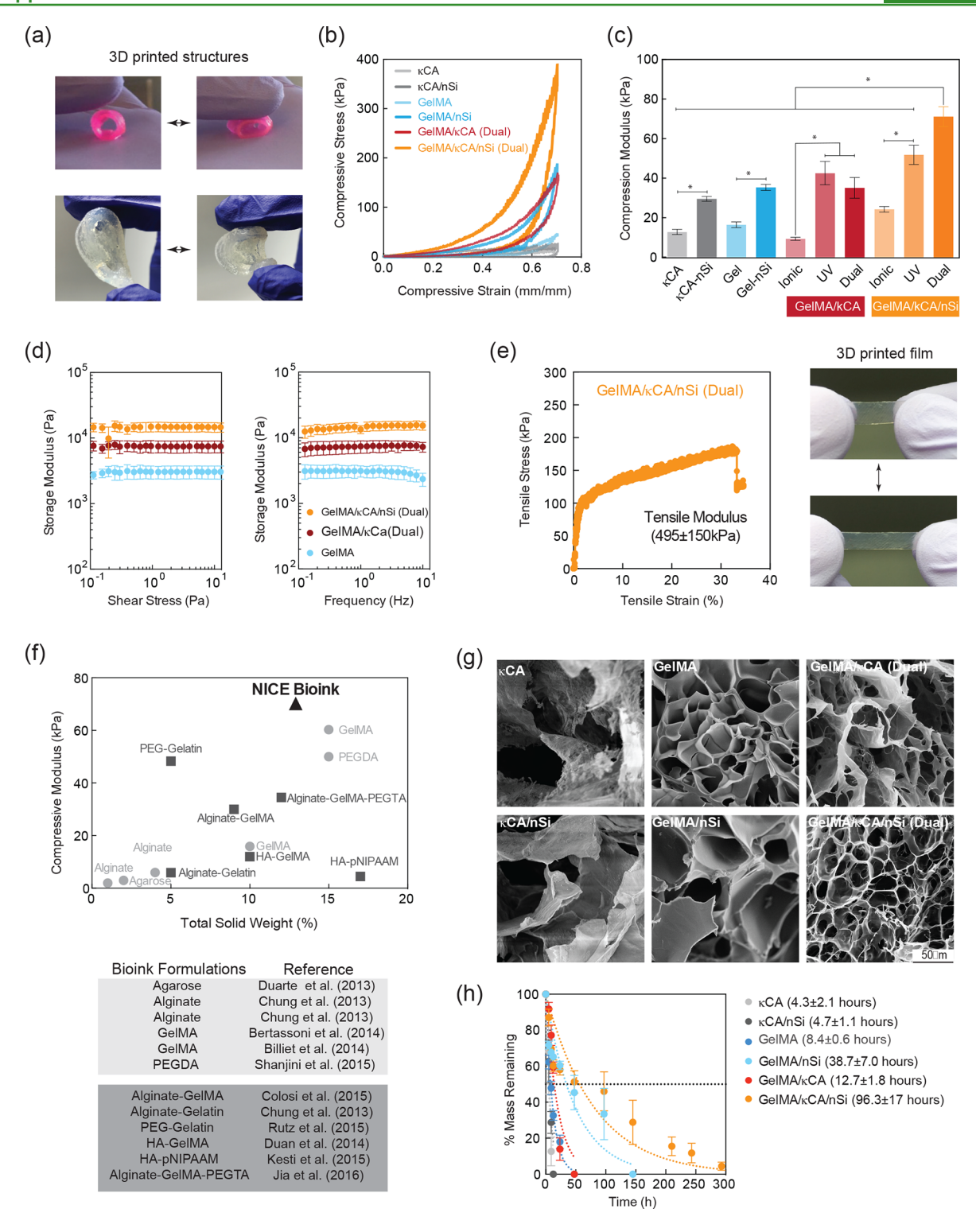


Figure 3. Effects of NICE reinforcement on mechanical properties after cross-linking. (a) The ability to be manually handles and compressed demonstrates the resilience and elasticity of cross-linked NICE structures. (b) The cyclic compression to 70% strain demonstrates NICE reinforcement's synergistic effect on mechanical strength compared to either single reinforcement mechanism, ICE (GelMA/ κ CA) and nanocomposite-(κ CA/nSi and GelMA/nSi) as well as individual polymeric hydrogels (κ CA, GelMA) (n=5). (c) The compression moduli data summarized for NICE and component hydrogels (n=5). The ionic and UV columns represent ICE networks with only a single network cross-linked: UV light cross-links only GelMA, while ionic solutions only cross-link κ CA. (d) Shear stress and frequency sweeps measure hydrogel storage moduli from 0.1 to 10 Pa and 0.1 to 10 Hz (n=3). (e) The tensile stress testing of bioprinted NICE segments failure. Manual extension demonstrates the elasticity of the NICE bioink. (f) Compressive modulus of various bioinks plotted with respect to total polymer weight. NICE bioink outperforms all other bioinks in terms of mechanical stiffness. (g) SEM imaging showing the porous microstructure of each cross-linked hydrogel. (h) The degradation kinetics of hydrogels tested under accelerated conditions (n=5). The degradation was accelerated using a heightened concentration of collagenase II, which enzymatically degrades GelMA.

Y-shaped bifurcated blood vessel was printed through a 400 μ m diameter tip (each layer height: ~200 μ m, extrusion width: ~500 μ m) to a height of 2 cm (100 layers) with 5 mm lumen diameter and 1 mm wall thickness (Figure S7). It is important to note that the difference between extruded width and tip diameter are caused by adjusting the rate of extrusion relative to printer movement speed, in order to match desired dimensions. The 500 μ m extruded line width used here is comparable to or better than that bioprinted lines using GelMA-alginate blends, ¹² hyaluronic acid and methacrylated hyaluronic acid, ¹⁴ gelatin with PEGX cross-linker, ⁷ gelatin with alginate, ⁸ gelatin and alginate with PEG cross-linkers, ¹⁵ methacrylated hyaluronic acid, ¹⁰ and GelMA reinforced with coprinted poloxamer ⁴² (Figure S8).

We attribute the superior printability of NICE bioink to the physical gelation of GelMA during the printing process in combination with the rheological effects of κ CA and nanosilicates. GelMA is fluidic above gelation temperature (\sim 30 °C), whereas it solidifies below gelation temperature. We printed NICE bioink above the gelation temperature (37 °C) onto a printing bed which is kept below the gelation temperature (25 °C). We performed a peak-hold test using a rheometer to mimic the flow behavior and temperature profile of bioink during the printing process (Figure S9). Our results show that the NICE bioink quickly solidifies after extrusion, which improves print fidelity and construct stability.

Physiologically relevant anatomical shapes such as a humansized ear were also printed using NICE bioink (Figure S7). These printability results represent a significant advancement over conventional bioinks in terms of both total height and aspect-ratio for freestanding bioprinted structures. 4,6,7,43 The development of this NICE bioink allows for a simple and direct approach to 3D printing of large biomimetic structures by improving Z-axis printability, and provides a platform technology for the creation of future bioactive bioinks. Further, combining the computational approach with experimental validation as described here can be used in the future to develop a more rational approach to the design of advanced bioinks. 5,6

NICE Reinforcement Improves Post-cross-linked Bioink Mechanical Properties. Mechanical properties of 3Dbioprinted structures are critical for maintaining the structural integrity of the scaffold and controlling cell behaviors including proliferation and differentiation.⁴ Nevertheless, many 3Dprinted structures using conventional bioinks are mechanically weak and lack appropriate elastomeric characteristics due to their chemical structure as well as poor interlayer cohesion. In contrast, the NICE dual-cross-linked bioprinted constructs were shown to be resilient under mechanical loading and to withstand severe mechanical deformation without delamination of printed layers (Figure 3a). We compared the effects of individual components and strengthening mechanisms on the mechanical properties of cross-linked hydrogels (GelMA, GelMA/nSi, κ CA, κ CA/nSi, GelMA/ κ CA, and GelMA/ κ CA/ nSi). Hydrogels containing GelMA were covalently cross-linked with UV light (25 mW/cm² of 365 nm) for 80 s, while hydrogels containing κCA were immersed in a 5% KCl solution to obtain ionically cross-linked networks. Because the GelMA/ κCA/nSi (NICE bioink) and GelMA/κCA have both ionic and covalently cross-linkable networks, they were tested with both networks cross-linked (dual-cross-linking), and with only a single network cross-linked (ionic or UV only). This allowed us

to isolate the effect of cross-linking from each polymer's presence alone.

We used uniaxial cyclic compression to determine compressive modulus and maximum stress at 70% strain of hydrogel formulations. The stress-strain compression data indicates that all hydrogel compositions containing GelMA can sustain 70% strain without fracture (Figure 3b, Figures S10 and S11). The results also revealed that the dual-cross-linked NICE bioink (71.1 ± 4.9 kPa) had a 4-fold higher compressive modulus than GelMA alone (16.5 \pm 1.5 kPa) and 2-fold higher modulus than either the GelMA/nSi nanocomposite (35.3 \pm 1.5 kPa) or GelMA/ κ CA ICE network (35.1 \pm 5.2 kPa) (Figure 3c). This pattern of synergistic reinforcement of NICE bioink was consistent for maximum stress at 70% strain (301.7 ± 21.0 kPa) compared to individual reinforcing mechanisms. Similarly, stress and frequency sweep results showed that NICE reinforcement (14.2 \pm 1.4 kPa) resulted in a storage modulus 4-fold higher than GelMA (3.1 \pm 0.3 kPa) and 2-fold higher than GelMA/ κ CA (7.4 \pm 0.9 kPa) (Figure 3d, Figure S12). We also investigated the elastomeric characteristics of the NICE bioink via 5-cycle compression tests to 40% compressive strain (Figure S10). Ionically cross-linked networks (κ CA and κ CA/ nSi) exhibited high plastic deformation (<30% recovery), particularly during the first cycle, while covalently cross-linked networks (GelMA and GelMA/nSi) showed high recovery (>90%). Both ICE (GelMA/ κ CA) and NICE (GelMA/ κ CA/ nSi) showed >75% recovery after cyclic deformation. Although NICE bioinks show reduced recovery, their energy dissipated per cycle remained higher than that for ICE and nanocomposites reinforced bioinks even after 5 cycles, demonstrating that NICE reinforcement is stable over multiple cycles (Figures S10 and S11). Interestingly, recent evidence suggests that KCA ICE networks can completely recover from strain over time as the ionic network reforms, although this is outside the scope of this study. 30,31,44 In addition to being able to sustain compression, a 3D-printed NICE film could sustain stretching and had a high tensile modulus (495 \pm 150 kPa) (Figure 3e). These tests confirm that combining ICE and nanocomposite reinforcement mechanisms results in a synergistic improvement in mechanical properties that translates into mechanically strong and resilient bioprinted structures.

The most common technique for improving hydrogel printability and mechanical strength is increasing cross-linking density and polymer concentration, however this approach also reduces hydrogel porosity and water content, limiting its suitability for bioprinting encapsulated cells. 4,6 Earlier studies have investigated polymers such as GelMA, 45 alginate, 46 agarose, 47 and PEG, 48 or polymer blends such as alginate-gelatin, 46 alginate-GelMA, 12 PEG-gelatin, 7 hyaluronic acid (HA)-GelMA, 13 HA-poly(N-isopropylacrylamide) (pNI-PAAM),¹⁴ and alginate-GelMA-PEG¹⁵ for bioprinting. Although some of these inks can provide suitable mechanical stiffness, their 3D printability remains limited, and their suitability as bioinks can be compromised due to high polymer concentrations (Figure 3f).^{4,6} The NICE bioink formulation overcomes this limitation by combining multiple reinforcement techniques to create mechanically stiff and elastomeric 3D printed structures where, unlike conventional reinforcement by increasing polymer content, 4,25 the mechanical improvements from the ICE and nanocomposite strengthening mechanisms are not due to a decrease in mesh size or hydration degree.

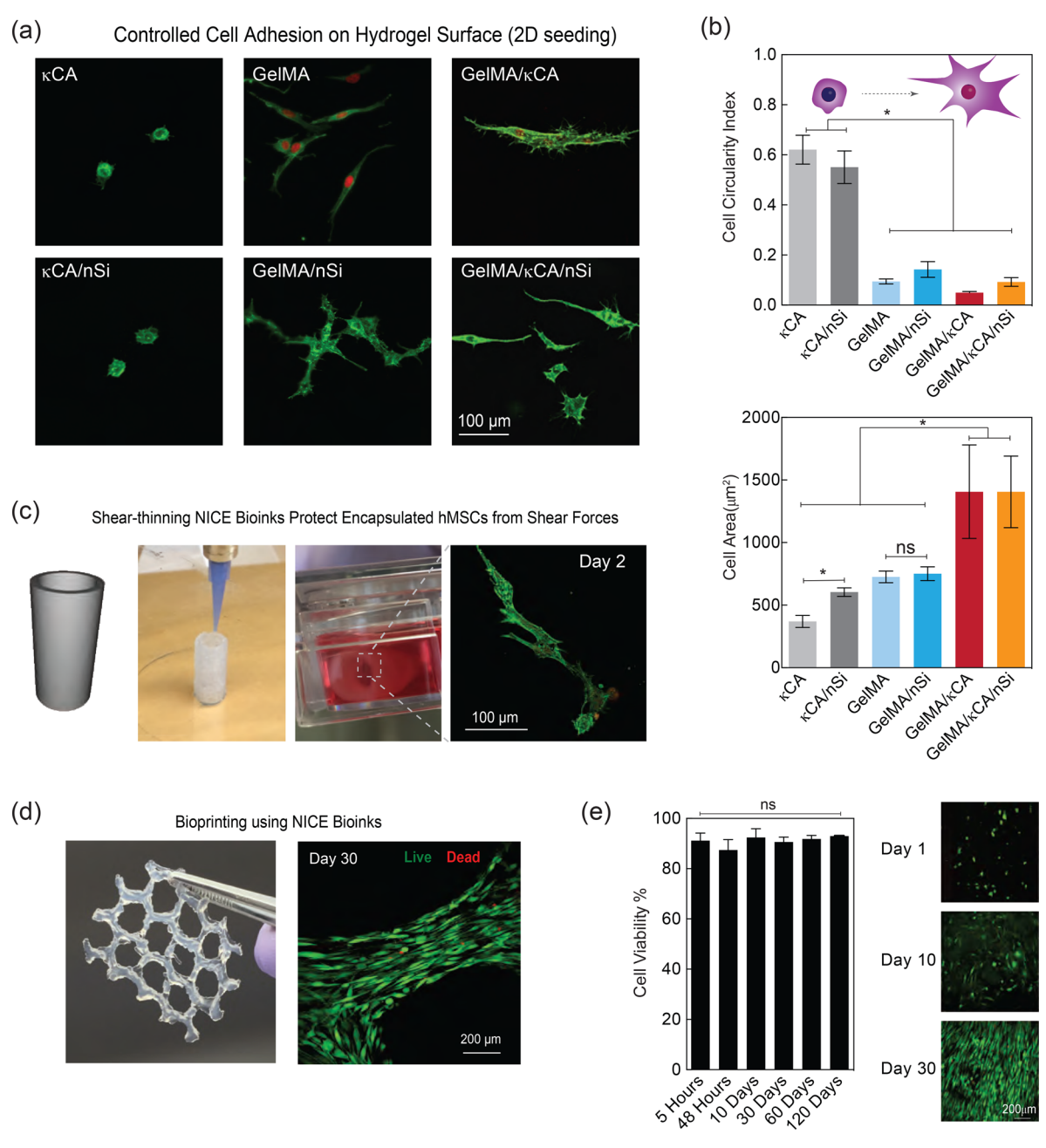


Figure 4. Bioprinting using NICE bioink. (a) The cell adhesion characteristics of individual polymers (κ CA, GelMA), nanocomposites (κ CA/nSi and GelMA/nSi), ICE (GelMA/ κ CA) and NICE bioink (GelMA/ κ CA/nSi) were investigated (n = 3). (b) The addition of GelMA and nanosilicates significantly improved cell adhesion and spreading as determined by circularity index and area of adherent cells (n = 3). (c) Bioprinted NICE cylindrical structures show high cell spreading after 48 h. (d) The encapsulated cells aligning parallel to 3D printed NICE scaffold structures after 30 days in culture. (e) The printed structure shows high cell viability (>85%), indicating that our bioprinting process is biocompatible. Short-term (48 h.) cell viability indicates high cell survival throughout the bioprinting process, supporting predictions from earlier modeling that shear forces during extrusion would not cause significant mortality. Long-term viability and adhesion allows cells to interact with and remodel scaffolds over time (n = 3).

Scanning electron microscopy (SEM) imaging revealed that all formulations maintained highly interconnected porous networks with diameters of ~20–50 μ m (Figure 3g). Water content in NICE bioink (89.5 \pm 0.3%) was similar to that of GelMA/nSi nanocomposites (89.2 \pm 0.5%) and GelMA/ κ CA ICE network (91.6 \pm 0.8%), which are also within the typical hydration range of many body tissues (Figure S13). Our results here demonstrated that the NICE bioink benefited from both ICE and nanoparticle reinforcement, with compressive moduli doubling with each reinforcement mechanism, and without

adverse effects on water content and pore size, which are both important measures of the suitability of a hydrogel for maintaining cell populations.

NICE reinforcing mechanisms improve physiological stability of 3D printed structures while retaining proteolytic functionality. Proteolytic degradation allows encapsulated cells to locally control degradation rates, allowing remodeling and migration to proceed on a cellular level. However, slow degradation kinetics are desirable for mechanical resilience during the initial phases of tissue remodeling. The physiological stability of the

NICE bioink was characterized by determining biodegradation/ dissolution kinetics as described in previous works. 33,49 A collagenase biodegradation assay was carried out in PBS with 2.5 U/mL collagenase type II to determine the susceptibility of the NICE bioink to cellular remodeling enzymes under accelerated conditions (Figure 3h). The amount of collagenase used here is much higher compared to in vivo or in vitro concentrations, and thus accelerates the enzymatic degradation of GelMA hydrogels. Compared to GelMA (half-life: 8.4 ± 0.6 h), GelMA/nSi (38.7 \pm 7.0 h) and GelMA/ κ CA (12.7 \pm 1.8 h) exhibited extended half-lives as measured by remaining hydrogel mass, which was further increased in the NICE bioink (96.3 \pm 17 h). These results are comparable to previous results on GelMA and GelMA nanosilicate degradation, and suggest that NICE reinforcement increases enzymatic stability even further. 33,49 Thus, NICE bioinks demonstrate a gradual rate of enzymatically driven degradation desirable for long-term tissue regeneration.

NICE Reinforced Scaffolds are Bioresponsive. The aim of 3D bioprinting is to regenerate functional tissues. In this regard, ECM derived bioinks are very promising because they support a wide array of cell-ECM interactions, enabling cell migration and remodeling and allowing bioinks to directly influence cell fate. GelMA's bioactivity has been thoroughly investigated in earlier studies, ^{26,27,50} so here the NICE bioink is compared to component gels to ensure key favorable cellmaterial interactions are maintained. We investigated the cellmaterial interactions of the bioink formulations by characterizing murine 3T3 preosteoblast adhesion to the surface of the various gel formulations. This cell line was used because previous studies have suggested that nanosilicates may promote osteogenesis, which is a future research avenue for bioprinted NICE structures. 33,49,51 Assessment of the extent of cell spreading was quantified by circularity index and cell size. This analysis demonstrated that cells on hydrogels containing GelMA (GelMA, GelMA/nSi, GelMA/κCA, and GelMA/κCA/ nSi) elongated significantly, although those on κ CA or κ CA/ nSi did not elongate (Figure 4a, b). This indicated that GelMA is responsible for cell adhesion and presence of κ CA and nanosilicates in NICE bioink does not interfere with the ability of GelMA to support cell adhesion. The addition of nanosilicates had a modest effect on overall cell spreading in κ CA hydrogels (κ CA/nSi), whereas both ICE (GelMA/ κ CA) and NICE (GelMA/κCA/nSi) networks supported much higher cell spreading due to the presence of GelMA. GelMA contains cell adhesion sites to support strong cell-matrix adhesions, but the extent of spreading is also proportional to substrate rigidity.⁵² Because the concentration of GelMA is similar in these formulations, the increase in cell area is likely due to increased mechanical stiffness in these networks. These results demonstrated that the NICE bioink maintains GelMA's bioactivity.53

To investigate the feasibility of this NICE ink for bioprinting applications involving cell-laden bioinks, we encapsulated cells within the NICE bioink and printed 3D constructs (cylinders with 1 cm diameter, 1 mm wall thickness, and a height of 2 cm) as well as honeycomb patterns (regular hexagon 5 mm edges, 1 mm thick walls). The honeycomb pattern was chosen as a low-infill density pattern to demonstrate the mechanical properties of a cross-linked NICE biostructure (Figure 4c, d). Initially (Day 1), uniform distribution of cells in the 3D printed scaffold was observed. These results support our modeling data that plug flow conditions during extrusion shield the cells from

shear forces during extrusion. At a later time point, the encapsulated cells proliferated and started to spread quickly along the long axis of the bioink filaments. Subsequently, cells started to migrate to the surface of bioprinted structure due to enhanced nutrition and cell numbers visibly increased until the scaffold surface was saturated with cells. Deeper areas within the thick cylindrical scaffold retained high cell viability and spreading, but lower cell density when observed with confocal microscopy. This is likely due to reduced nutrient diffusion deeper into the scaffold. These data show that bioprinted NICE scaffolds are cytocompatible for long-term culture.

Cell viability was high (>90%) immediately after 3D bioprinting (Figure 4e). The encapsulated cells remained viable throughout the 120-day observation period. Proliferation of encapsulated cells was also observed by live/dead imaging over multiple days (day 1, 10, and 30) (Figure S5). Z-Stack confocal images of a 3D bioprinted cylindrical structure illustrated an increase in cell density. We observed that initially (day 0), the printed construct was translucent, but it slowly turned opaque (day 30) due to deposition of ECM by encapsulated cells. The cell-laden printed structure maintained its structural integrity, indicating that the GelMA degradation rate was matched by ECM deposition by cells.

Overall, these results show that the NICE bioink supports high cell viability, attachment, and proliferation, indicating high cytocompatibility. Our earlier studies have shown that nanosilicate based hydrogels are biocompatible using subcutaneous nanosilicate injections, which resulted in only mild local inflammation and no signs of systemic inflammation.³⁵ In addition, gelatin-nanosilicate hydrogels were almost completely resorbed at 28 days under in vivo conditions. The precise mechanism of nanosilicate clearance has not been completely elucidated, but it is suspected that the nanoparticles are degraded into nontoxic components.^{35,36,54} Thus, it is expected that NICE bioink can be used to print custom scaffolds to promote tissue regeneration in non-load-bearing regions.

CONCLUSION

In this study, we introduced a novel reinforcement technique, nanoengineered ionic covalent entanglement (NICE), to engineer an advanced bioactive bioink with superior printability and mechanical properties. The NICE bioink can be used to print freestanding, high aspect-ratio structures over 3 cm and 150 layers tall with excellent shape fidelity, and the structures become tough and elastic after cross-linking. Meanwhile, bioprinted cells maintained high viability, attachment, and spreading throughout the 120-day period. We used a Herschel-Bulkley computational model incorporating rheological data on yield point, consistency, and shear thinning characteristics to simulate bioink behavior and predict the shear stresses cells experience during bioprinting. The Herschel-Bulkley fluid behavior of the NICE bioink may explain the improved 3D printability and plug flow that shields bioprinted cells from shear stresses under extrusion conditions. This model can be used to identify print parameters that maximize printability. The NICE bioink demonstrated here was developed as a platform technology, intended to provide researchers with a facile technique for bioprinting larger 3D tissue scaffolds without requiring costly multiheaded printing systems. Future work will investigate a broader range of material compositions to customize NICE bioinks for specific applications and tissue types. Upcoming NICE bioink developments also include localizing bioactive cues within scaffolds to spatially direct cell behavior, and arranging multiple cell types and concentrations within scaffolds to replicate multilayered tissues like cartilage and blood vessels. These approaches could enable precise spatial control over cell behavior within human-scale bioprinted structures, bringing bioprinting closer to the goal of recreating functional human tissues. The NICE bioink is unique among existing bioinks because it combines superior printability, improved mechanical properties, and excellent bioactivity into a single bioink formulation. This represents a significant advance in bioink technology, and will prove to be a useful tool for researchers seeking to replicate human tissues using bioactive 3D structures.

EXPERIMENTAL SECTION

Materials Synthesis. The porcine gelatin (Bloom No. 300, Type A), Irgacure2959 (2-Hydroxy-4'-(2-hydroxyethoxy)-2-methylpropiophenone), and methacrylic anhydride were purchased from Sigma-Aldrich (USA). Kappa-carrageenan (κCA) was obtained from TCI America (USA). Nanosilicates (Laponite XLG) were obtained from BYK Additives Inc. Gelatin methacryloyl (GelMA) (80% methacrylated) was synthesized by dissolving 10 g of gelatin in 100 mL of phosphate buffered saline (PBS), then heating for 1 h at 60 °C. After dissolution, 8 mL of methacrylic anhydride was added dropwise over a period of minutes. The solution was kept at 60 °C for 3 h, then 400 mL of 1× PBS was added. The solution was dialyzed at 50 °C for 7 days and lyophilized. The NICE bioink (10%w/v GelMA, 1%w/v κCA, 2% w/v nanosilicates, and 0.25% w/v Irgacure2959) was obtained by 1:1 mixing of 20%w/v GelMA + 2%w/v KCA with a solution of 4% w/v nanosilicates +0.5% w/v Irgacure 2959. The solution was vortexed and subsequently sonicated for 2 min to ensure homogeneous dispersion of components. Solutions were stored overnight at 40 °C. The bioink was covalently cross-linked via exposure to 25 mW/cm² 365 nm UV light for 80 s. Ionic cross-linking was completed by submersion in 5% potassium chloride (KCl) for 30

Physiological Stability. Equilibrium hydration was calculated by soaking cross-linked gels in PBS overnight and obtaining their weights, then lyophilizing the gels and comparing dry weight to wet weight. Biodegradation rates were assessed in the presence of 2.5 U/mL Collagenase Type II (Worthington Biochemical Corporation). 150 μ L hydrogels (n=3) were cross-linked and placed in preweighed individual containers, then allowed to sit at room temperature overnight in 1X PBS to reach equilibrium. Fifteen hours later, the solution was replaced with 1× PBS with 2.5 U/mL Collagenase Type II and the hydrogels were stored in an incubator at 37 °C. The mass of hydrogel remaining was measured by carefully removing all solution from the container, then weighing the hydrogel together with the container as to not damage samples. Hydration percentages were calculated using the formula hydration (%) = [1 - (dry mass/wet mass)]100.

Microstructure. The morphology of the hydrogel was visualized via scanning electron microscope (SEM) using a NeoScope JCM-5000 SEM. Hydrogel samples were frozen in liquid nitrogen, cracked with a razor blade, and lyophilized. Samples were fixed and sputter-coated with gold to a thickness of 21 nm.

Rheological Characterization. Rheological testing was carried out on an Anton Paar Physica MCR-301 Rheometer, using a 10 mm PP10 measuring plate and 50 mm CP50–1 measuring plate. UV gelation, frequency sweeps, stress sweeps, shear stress sweeps, and shear rate sweeps were performed. For UV gelation, each hydrogel's time to gelation was tested by measuring changes in storage modulus while the gels were exposed to 15, 25, or 45 mW/cm2 of 365 nm UV light (Figure S2). Each covalently cross-linkable bioink was tested (*n* = 3) at 10 mm diameter × 0.5 mm thick. UV light was turned on at 30s and remained on for 300 s. The frequency sweep was carried out on cross-linked hydrogels at a stress of 1 Pascal (Pa) and covered a range of frequencies from 0.1 to 10 Hz. The stress sweep, also on cross-linked hydrogels, swept a range of shear stresses from 0.1 to 100 Pa at

a frequency of 1 Hz. Finally, stress and shear rate sweeps on non-cross-linked hydrogels were carried out sequentially to measure viscosity under a range of conditions designed to correspond to printing conditions. Shear stress was varied from 0.01 to 2000 Pa. Shear rates from 0.01 to 100 s⁻¹ were tested. Gels were kept in a high humidity atmosphere to prevent dehydration from affecting results.

Bioprinting. Printed shapes were designed in Solidworks and exported as STL files. STL files were loaded into Slic3r to customize printing options and converted into G-code printer instructions. Pronterface was used to interface with the 3D printer. Layer height was set to 200 μ m, layer width was set at 500 μ m, and print speed was kept at 20 mm/s, or 0.15 mL/min, for all trials. When necessary, 2 μ L/mL of plumbers tracing dye was added to enhance visualization. The bioink was stored at 37 °C and loaded into an extrusion tube with a 400 μ m nozzle tip and extrusion printed through an I3 RepRap printer. Using these settings, a hollow 2 cm tall x OD 10 mm ID 8 mm cylinder was printed from the bioink. A bifurcated branching blood vessel shape was printed with interior diameter of 5 mm, wall thickness of 1 mm, and height of 1.5 cm.

Uniaxial Compression. Cast cross-linked hydrogel samples were cut into cylinders using a biopsy punch, making sample material cylinders 6 mm in diameter by 2.5 mm thick. Each sample was checked using digital calipers and the ADMET MTEST Quattro eXpert 7600, and variances in dimension were factored in to stress and strain calculations. Unconstrained samples were compressed and returned to starting position at 1 mm/min. Raw data for single cycle compression was processed using an Excel macro for compressive modulus (calculated from 0 to 20% strain region), and maximum stress at 70% strain. Raw data for multicycle compression (40% strain) was also processed to monitor compressive modulus, energy dissipated, and recovery using a separate macro. Compression data was taken for hydrogel samples of GelMA (10%), GelMA (10%)/nSi (2%), κCA (1%), $\kappa CA(1\%)/nSi(2\%)$, $GelMA(10\%)/\kappa CA(1\%)$, and GelMA(10%)/κCA(1%)/nSi(2%). Where applicable, gels were also tested as semi-interpenetrating networks (sIPNs) by cross-linking only one network.

Derivation of Model. The fully developed velocity profile for a Herschel-Bulkley fluid flowing in a tube was derived using the conservation of momentum equations in cylindrical coordinates. For laminar, isothermal flow of an incompressible fluid with no-slip boundary conditions, the equations describing flow in the r and θ directions simplified to 0, leaving only the equations describing flow in the z direction (eq 1).

$$\begin{split} \rho \left(\frac{\delta u_z}{\delta t} + u_r \frac{\delta u_z}{\delta r} + \frac{u_\theta}{r} \frac{\delta u_z}{\delta \theta} + u_z \frac{\delta u_z}{\delta z} \right) \\ &= \rho g_z - \frac{\partial P}{\partial z} + \left(\frac{1}{r} \frac{\delta (r \tau_{rz})}{\delta r} + \frac{1}{r} \frac{\delta (\tau_{\theta z})}{\delta \theta} + \frac{\delta (\tau_{zz})}{\delta z} \right) \end{split} \tag{1}$$

Under steady-state, with only axially directed flow, the equation further simplifies to eq 2.

$$\frac{\partial P}{\partial z} - \rho g_z = \frac{\Delta P}{L} = \frac{1}{r} \frac{\delta(r\tau_{rz})}{\delta r} \tag{2}$$

Integration with respect to r yields eq 4, which reaches a maximum at the wall (r = R).

$$\tau_{rz} = \frac{r}{2} \frac{\Delta P}{L} \tag{3}$$

$$\tau_{wall} = \frac{R}{2} \frac{\Delta P}{L} \tag{4}$$

Combining eqs 3 and 4 and relating the result to the Herschel-Bulkley model gives eq 5.

$$\tau_{rz} = \tau_0 + k\dot{\gamma}^n = \frac{r}{R}\tau_{\text{wall}} \tag{5}$$

Solving for shear rate $(\dot{\gamma} = \frac{\partial u_z(r,\theta)}{\partial r})$ and noting the plug flow region $(0 \le r \le R_0)$ gives eq 6.

$$\frac{\partial u_z(r,\theta)}{\partial r} = \begin{cases}
0, 0 < r < R_0 \\
\left(\frac{\tau_{\text{wall}}}{k}\right)^{1/n} \left(\frac{r}{R} - \frac{\tau_0}{\tau_{\text{wall}}}\right)^{1/n}, R_0 \le r \le R
\end{cases}$$
(6)

Integration yields the velocity profile (eq 7) which describes the velocity profile:

$$\begin{split} u_z(r,\,\theta) &= \int \frac{\partial u_z(r,\,\theta)}{\partial r} \partial r \\ &= \begin{cases} R\bigg(\frac{n}{n+1}\bigg)\bigg(\frac{\tau_{\text{wall}}}{k}\bigg)^{1/n}\bigg(1-\frac{\tau_0}{\tau_{\text{wall}}}\bigg)^{n+1/n} & 0 < r < R_0 \\ R\bigg(\frac{n}{n+1}\bigg)\bigg(\frac{\tau_{\text{wall}}}{k}\bigg)^{1/n}\bigg(\bigg(1-\frac{\tau_0}{\tau_{\text{wall}}}\bigg)^{n+1/n} \\ -\bigg(\frac{r}{R}-\frac{\tau_0}{\tau_{\text{wall}}}\bigg)^{n+1/n} \bigg) & R_0 \leq r \leq R \end{cases} \end{split}$$

Integration across the tube yields the volumetric flow rate (eq 8).

$$Q = \int_0^R u_z(r, \theta) dr$$

$$= \pi R^3 \left(\frac{n}{n+1}\right) \left(\frac{\tau_{\text{wall}}}{k}\right)^{1/n} \left(1 - \frac{\tau_0}{\tau_{\text{wall}}}\right)^{n+1/n}$$

$$\left(1 - \frac{2n}{(2n+1)(3n+1)} \left(1 - \frac{\tau_0}{\tau_{\text{wall}}}\right) \left(\frac{\tau_0}{\tau_{\text{wall}}} n + 2n + 1\right)\right)$$
(8)

where $\frac{\partial u_z(r,\theta)}{\partial r}$ = shear rate, $u_z(r,\theta)$ = velocity, Q = volumetric flow rate, n = flow behavior index, k = flow consistency index, τ_0 = yield stress, R = inner radius of needle, L = length of needle, ΔP = applied pressure, τ_{wall} = stress at wall of needle, and R_0 = radius of plug flow region

Computational Modeling. The equations above were solved in Matlab (MathWorks, Natick, MA) to simulate extrusion through a needle. Because the flow rate of the print and the rheological constants were known, an iterative approach was used to find τ_{wall} from eq 8. Once τ_{wall} was determined, the velocity and shear rate profiles (eqs 6 and 7) could be easily plotted for all positions within the flow.

In Vitro Studies. To evaluate the hydrogel bioink's ability to culture cells, wer seeded murine 3T3 preosteoblasts (MC3T3-E1 Subclone 4, ATCC CRL-2593) on 3.5 cm diameter samples. MC3T3s were cultured on hydrogels of GelMA (10%), GelMA (10%)/nSi (2%), κ CA (1%), κ CA(1%)/nSi(2%), GelMA(10%)/ κ CA(1%), and GelMA(10%)/κCA(1%)/nSi(2%). All cells were used at passage 22 and 100 000 cells were seeded onto each gel sample. Cells were cultured in normal DMEM growth media with 10% FBS at 37 °C for 3 days. After 3 days, each hydrogel was triple rinsed with PBS, soaked with paraformaldehyde for 1.5 h, then triple rinsed again. Cells were then permeabilized by exposure to Triton X for 20 min and triple rinsed with PBS. One hundred microliters of phalloidin was added to each well plate, then stored at room temperature for 1 h. After triple rinsing with PBS, cells were incubated with RNase for 1 h at 37 °C, triple rinsed again, and incubated with propidium iodide at 37 °C for 20 min. Finally, cells were triple rinsed in PBS. Cells were imaged using confocal microscopy and EZC1 software. Images were taken as Z-stack.ids files, which were compiled into 3D models using EZC1 software, and compiled into focused 2D images using EZC1 or ImageJ via the bioformats import and stack focuser plugins. The circularity index on ImageJ was used to quantify a cell's deviation from a perfect circle, and the area size was also calculated using ImageJ. Images used in analysis were taken randomly of the surfaces of the 3 replicate scaffolds.

3D Bioprinting. Because the κ CA, κ CA/nSi, GelMA, GelMA/nSi, and GelMA/kCA all failed the standard cylinder test below 3 mm height, bioprinting was only attempted using the NICE bioink (GelMA/κCA/nSi). 1 ×10⁶ mouse preosteoblast MC3T3-E1 Subclone 4 (ATCC CRL-2593) cells were trypsinized for 5 min, 10 mL of media was then added, and the solution was centrifuged for 5 min. The supernatant was removed, and the cell pellet was resuspended in 200 uL of media. The resuspended solution was gently mixed into 2.8 mL of the NICE bioink at 37 °C by pipetting, for a final concentration of approximately 3.33 × 10⁵ cells/mL. The bioink was prepared using PBS to maximize cell viability. The bioink was then transferred into the extruder and printed into several constructs using the same print settings defined in the bioprinting section: a 400um tapering luer-lock nozzle, line width of 500um, a layer height of 200um, and a print speed of 0.15 mL/min. A hollow cylinder was printed with an outer diameter of 1 cm, inner diameter of 0.8 cm, and height of 2 cm. Four flat disc scaffolds 1 cm in diameter and 1 mm in height were also printed as replicates. These disc scaffolds (n = 3) used a 100% rectilinear infill, and were used to replicate the cell viability results. A honeycomb pattern was also used as a low-infill density pattern to demonstrate the mechanical properties of a cross-linked NICE biostructure. This pattern was a regular hexagon infill with 5 mm edges and 1 mm thick walls. All printing settings were kept consistent during bioprinting as described in the bioprinting section. All scaffolds (n = 3) were crosslinked using UV light as described above, and soaked in a 5% KCl solution for 5 min, then incubated in DMEM media with 10% FBS. The ionic cross-linking time was reduced relative to the molded bioinks because the bioprinted structures were thinner than the cylindrical samples used in the earlier experiments (1 mm thick vs 2.5 mm thick), and concurrent research determined that the 30 min crosslinking time was unnecessarily long.⁵⁵ Viability was analyzed using live/dead imaging was carried out by incubating cells in a PBS solution containing 1 µL/mL calcein AM and 2 µL/mL ethidium homodimer for 1 h, then soaking once in 1× PBS to limit background signal. Live/ dead measurements were taken at 5, 24, and 48 h, and 10, 30, 60, and 120 days (n = 3). Imaging was carried out using confocal microscopy with environment chamber: Z-Stack images were taken of 3 randomly selected surface areas and 1 cross-section of the 3D-bioprinted structures. Z-stack images were taken to a depth of 400 um using a confocal microscope and processed using EZC1 and ImageJ to count total number of living and dead cells within each 3D section of the biostructure.

Statistical Analysis. The quantitative experimental results were analyzed and graphed as mean \pm standard deviation. Statistical analysis of all quantitative data was performed using one-way analysis of variance (ANOVA), and pairwise data comparison was done via Bonferroni's multiple comparison test. Statistical significance was shown as *p < 0.05, **p < 0.01, and ***p < 0.001.

ASSOCIATED CONTENT

S Supporting Information

The Supporting Information is available free of charge on the ACS Publications website at DOI: 10.1021/acsami.7b19808.

Experimental data from dynamic light scattering (DLS), electrophoretic mobility, rheology, uniaxial compression, and hydration degree (PDF)

AUTHOR INFORMATION

Corresponding Author

*E-mail: gaharwar@tamu.edu. Address: 3120 TAMU, 5024 Emerging Technology Building, College Station, TX 77843-3120. Telephone: (979) 458-5540. Fax: (979) 845-4450.

ORCID

Akhilesh K. Gaharwar: 0000-0002-0284-0201

Author Contributions

D.C. and A.K.G. designed the experiments and wrote the manuscript. C.W.P contributed to rheological studies, J.L.G. contributed to computational modeling of Herschel-Bulkley model, J.K.C., L.M.C., E.M., and G.B.C.C. contributed to in vitro studies. All authors have given approval to the final version of the manuscript.

Fundina

A.K.G. acknowledges financial support from National Science Foundation (CBET 1705852).

Notes

The authors declare the following competing financial interest(s): Provisional patent application USSN 62/470,727, Nanocomposite Ionic-Covalent Entanglement Reinforcement Mechanism and Hydrogel.

ACKNOWLEDGMENTS

We Elsy Rivero and Adrian Olivera from Universidad Modelo (Mexico) and Ashwathi Nair (Texas A&M University) for helping in optimizing printing parameters and bioink formulations, and Dr. Manish K. Jaiswal for transmission electron microscopy (TEM) of nanosilicates. We also thank Dr. Nicholas A. Sears for helping to troubleshoot the 3D printer.

REFERENCES

- (1) Murphy, S. V.; Atala, A. 3D bioprinting of tissues and organs. *Nat. Biotechnol.* **2014**, 32 (8), 773–785.
- (2) Derby, B. Printing and prototyping of tissues and scaffolds. *Science* **2012**, 338 (6109), 921–926.
- (3) Khademhosseini, A.; Langer, R. A decade of progress in tissue engineering. *Nat. Protoc.* **2016**, *11* (10), 1775–1781.
- (4) Malda, J.; Visser, J.; Melchels, F. P.; Jüngst, T.; Hennink, W. E.; Dhert, W. J. A.; Groll, J.; Hutmacher, D. W. 25th Anniversary Article: Engineering Hydrogels for Biofabrication. *Adv. Mater.* **2013**, *25* (36), 5011–5028.
- (5) Farahani, R. D.; Dubé, M.; Therriault, D. Three-Dimensional Printing of Multifunctional Nanocomposites: Manufacturing Techniques and Applications. *Adv. Mater.* **2016**, *28* (28), 5794–5821.
- (6) Chimene, D.; Lennox, K. K.; Kaunas, R. R.; Gaharwar, A. K. Advanced Bioinks for 3D Printing: A Materials Science Perspective. *Ann. Biomed. Eng.* **2016**, *44*, 2090–2102.
- (7) Rutz, A. L.; Hyland, K. E.; Jakus, A. E.; Burghardt, W. R.; Shah, R. N. A Multimaterial Bioink Method for 3D Printing Tunable, Cell-Compatible Hydrogels. *Adv. Mater.* **2015**, *27* (9), 1607–1614.
- (8) He, Y.; Yang, F.; Zhao, H.; Gao, Q.; Xia, B.; Fu, J. Research on the printability of hydrogels in 3D bioprinting. *Sci. Rep.* **2016**, *6*, 29977.
- (9) Liu, W.; Zhang, Y. S.; Heinrich, M. A.; De Ferrari, F.; Jang, H. L.; Bakht, S. M.; Alvarez, M. M.; Yang, J.; Li, Y.-C.; Trujillo-de Santiago, G.; Miri, A. K.; Zhu, K.; Khoshakhlagh, P.; Prakash, G.; Cheng, H.; Guan, X.; Zhong, Z.; Ju, J.; Zhu, G. H.; Jin, X.; Shin, S. R.; Dokmeci, M. R.; Khademhosseini, A. Rapid Continuous Multimaterial Extrusion Bioprinting. Adv. Mater. 2017, 29 (3), 1604630.
- (10) Ouyang, L.; Highley, C. B.; Sun, W.; Burdick, J. A. A Generalizable Strategy for the 3D Bioprinting of Hydrogels from Nonviscous Photo-crosslinkable Inks. *Adv. Mater.* **2017**, 29 (8), 1604983.
- (11) Highley, C. B.; Rodell, C. B.; Burdick, J. A. Direct 3D printing of shear-thinning hydrogels into self-healing hydrogels. *Adv. Mater.* **2015**, 27 (34), 5075–5079.
- (12) Colosi, C.; Shin, S. R.; Manoharan, V.; Massa, S.; Costantini, M.; Barbetta, A.; Dokmeci, M. R.; Dentini, M.; Khademhosseini, A. Microfluidic Bioprinting of Heterogeneous 3D Tissue Constructs Using Low-Viscosity Bioink. *Adv. Mater.* **2016**, 28 (4), 677–684.
- (13) Duan, B.; Kapetanovic, E.; Hockaday, L. A.; Butcher, J. T. Three-dimensional printed trileaflet valve conduits using biological

- hydrogels and human valve interstitial cells. Acta Biomater. 2014, 10 (5), 1836–1846.
- (14) Kesti, M.; Müller, M.; Becher, J.; Schnabelrauch, M.; D'Este, M.; Eglin, D.; Zenobi-Wong, M. A versatile bioink for three-dimensional printing of cellular scaffolds based on thermally and photo-triggered tandem gelation. *Acta Biomater.* **2015**, *11*, 162–172.
- (15) Jia, W.; Gungor-Ozkerim, P. S.; Zhang, Y. S.; Yue, K.; Zhu, K.; Liu, W.; Pi, Q.; Byambaa, B.; Dokmeci, M. R.; Shin, S. R.; Khademhosseini, A. Direct 3D Bioprinting of Perfusable Vascular Constructs Using a Blend Bioink. *Biomaterials* **2016**, *106*, 58.
- (16) Bootsma, K.; Fitzgerald, M. M.; Free, B.; Dimbath, E.; Conjerti, J.; Reese, G.; Konkolewicz, D.; Berberich, J. A.; Sparks, J. L. 3D printing of an interpenetrating network hydrogel material with tunable viscoelastic properties. *J. Mech. Behavior Biomed. Mater.* **2017**, *70*, 84.
- (17) Kolesky, D. B.; Truby, R. L.; Gladman, A.; Busbee, T. A.; Homan, K. A.; Lewis, J. A. 3D bioprinting of vascularized, heterogeneous cell-laden tissue constructs. *Adv. Mater.* **2014**, *26* (19), 3124–3130.
- (18) Wilson, S. A.; Cross, L. M.; Peak, C. W.; Gaharwar, A. K. Shear-Thinning and Thermo-Reversible Nanoengineered Inks for 3D Bioprinting. ACS Appl. Mater. Interfaces 2017, 9 (50), 43449–43458.
- (19) Peak, C. W.; Stein, J.; Gold, K. A.; Gaharwar, A. K. Nanoengineered Colloidal Inks for 3D Bioprinting. *Langmuir* **2018**, 34 (3), 917–925.
- (20) Gaharwar, A. K.; Peppas, N. A.; Khademhosseini, A. Nanocomposite hydrogels for biomedical applications. *Biotechnol. Bioeng.* **2014**, *111* (3), 441–453.
- (21) Wang, Q.; Mynar, J. L.; Yoshida, M.; Lee, E.; Lee, M.; Okuro, K.; Kinbara, K.; Aida, T. High-water-content mouldable hydrogels by mixing clay and a dendritic molecular binder. *Nature* **2010**, *463* (7279), 339–343.
- (22) Sun, J.-Y.; Zhao, X.; Illeperuma, W. R.; Chaudhuri, O.; Oh, K. H.; Mooney, D. J.; Vlassak, J. J.; Suo, Z. Highly stretchable and tough hydrogels. *Nature* **2012**, *489* (7414), 133–136.
- (23) Bakarich, S. E.; Panhuis, M. i. h.; Beirne, S.; Wallace, G. G.; Spinks, G. M. Extrusion printing of ionic-covalent entanglement hydrogels with high toughness. *J. Mater. Chem. B* **2013**, *I* (38), 4939–4946.
- (24) Shull, K. R. Materials science: A hard concept in soft matter. *Nature* **2012**, 489 (7414), 36–37.
- (25) Matricardi, P.; Di Meo, C.; Coviello, T.; Hennink, W. E.; Alhaique, F. Interpenetrating Polymer Networks polysaccharide hydrogels for drug delivery and tissue engineering. *Adv. Drug Delivery Rev.* **2013**, *65* (9), 1172–1187.
- (26) Yue, K.; Trujillo-de Santiago, G.; Alvarez, M. M.; Tamayol, A.; Annabi, N.; Khademhosseini, A. Synthesis, properties, and biomedical applications of gelatin methacryloyl (GelMA) hydrogels. *Biomaterials* **2015**, 73, 254–271.
- (27) Klotz, B. J.; Gawlitta, D.; Rosenberg, A. J.; Malda, J.; Melchels, F. P. Gelatin-Methacryloyl Hydrogels: Towards Biofabrication-Based Tissue Repair. *Trends Biotechnol.* **2016**, 34 (5), 394–407.
- (28) Jabbari, E.; Leijten, J.; Xu, Q.; Khademhosseini, A. The matrix reloaded: the evolution of regenerative hydrogels. *Mater. Today* **2016**, *19* (4), 190–196.
- (29) Mangione, M. R.; Giacomazza, D.; Bulone, D.; Martorana, V.; Cavallaro, G.; San Biagio, P. L. K+ and Na+ effects on the gelation properties of κ-Carrageenan. *Biophys. Chem.* **2005**, *113* (2), 129–135.
- (30) Liu, S.; Li, L. Recoverable and Self-Healing Double Network Hydrogel Based on κ-Carrageenan. ACS Appl. Mater. Interfaces 2016, 8 (43), 29749–29758.
- (31) Stevens, L.; Calvert, P.; Wallace, G. G.; in het Panhuis, M. Ionic-covalent entanglement hydrogels from gellan gum, carrageenan and an epoxy-amine. *Soft Matter* **2013**, *9* (11), 3009–3012.
- (32) Chimene, D.; Alge, D. L.; Gaharwar, A. K. Two-Dimensional Nanomaterials for Biomedical Applications: Emerging Trends and Future Prospects. *Adv. Mater.* **2015**, 27 (45), 7261–7284.
- (33) Xavier, J. R.; Thakur, T.; Desai, P.; Jaiswal, M. K.; Sears, N.; Cosgriff-Hernandez, E.; Kaunas, R.; Gaharwar, A. K. Bioactive

- nanoengineered hydrogels for bone tissue engineering: a growth-factor-free approach. ACS Nano 2015, 9 (3), 3109–3118.
- (34) Thakur, A.; Jaiswal, M. K.; Peak, C. W.; Carrow, J. K.; Gentry, J.; Dolatshahi-Pirouz, A.; Gaharwar, A. K. Injectable shear-thinning nanoengineered hydrogels for stem cell delivery. *Nanoscale* **2016**, 8, 12362–12372.
- (35) Gaharwar, A. K.; Avery, R. K.; Assmann, A.; Paul, A.; McKinley, G. H.; Khademhosseini, A.; Olsen, B. D. Shear-Thinning Nanocomposite Hydrogels for the Treatment of Hemorrhage. *ACS Nano* **2014**, *8* (10), 9833–9842.
- (36) Ghadiri, M.; Chrzanowski, W.; Rohanizadeh, R. Antibiotic eluting clay mineral (Laponite®) for wound healing application: An in vitro study. *J. Mater. Sci.: Mater. Med.* **2014**, *25* (11), 2513–2526.
- (37) Klein, A.; Whitten, P. G.; Resch, K.; Pinter, G. Nanocomposite hydrogels: Fracture toughness and energy dissipation mechanisms. *J. Polym. Sci., Part B: Polym. Phys.* **2015**, *53* (24), 1763–1773.
- (38) Mouser, V. H.; Melchels, F. P.; Visser, J.; Dhert, W. J.; Gawlitta, D.; Malda, J. Yield stress determines bioprintability of hydrogels based on gelatin-methacryloyl and gellan gum for cartilage bioprinting. *Biofabrication* **2016**, *8* (3), 035003.
- (39) Sathaye, S.; Mbi, A.; Sonmez, C.; Chen, Y.; Blair, D. L.; Schneider, J. P.; Pochan, D. J. Rheology of peptide-and protein-based physical hydrogels: Are everyday measurements just scratching the surface? WIREs: Nanomedicine and Nanobiotechnology 2015, 7 (1), 34–68
- (40) Marquardt, L. M.; Heilshorn, S. C. Design of Injectable Materials to Improve Stem Cell Transplantation. *Curr. Stem Cell Rep.* **2016**, 207–220.
- (41) Nair, K.; Gandhi, M.; Khalil, S.; Yan, K. C.; Marcolongo, M.; Barbee, K.; Sun, W. Characterization of cell viability during bioprinting processes. *Biotechnol. J.* **2009**, *4* (8), 1168–1177.
- (42) Melchels, F. P.; Blokzijl, M. M.; Levato, R.; Peiffer, Q. C.; De Ruijter, M.; Hennink, W. E.; Vermonden, T.; Malda, J. Hydrogel-based reinforcement of 3D bioprinted constructs. *Biofabrication* **2016**, 8 (3), 035004.
- (43) Kang, H.-W.; Lee, S. J.; Ko, I. K.; Kengla, C.; Yoo, J. J.; Atala, A. A 3D bioprinting system to produce human-scale tissue constructs with structural integrity. *Nat. Biotechnol.* **2016**, 34 (3), 312–319.
- (44) Lu, X.; Chan, C. Y.; Lee, K. I.; Ng, P. F.; Fei, B.; Xin, J. H.; Fu, J. Super-tough and thermo-healable hydrogel promising for shape-memory absorbent fiber. *J. Mater. Chem. B* **2014**, 2 (43), 7631–7638.
- (45) Bertassoni, L. E.; Cardoso, J. C.; Manoharan, V.; Cristino, A. L.; Bhise, N. S.; Araujo, W. A.; Zorlutuna, P.; Vrana, N. E.; Ghaemmaghami, A. M.; Dokmeci, M. R.; Khademhosseini, A. Direct-write bioprinting of cell-laden methacrylated gelatin hydrogels. *Biofabrication* **2014**, *6* (2), 024105.
- (46) Chung, J. H.; Naficy, S.; Yue, Z.; Kapsa, R.; Quigley, A.; Moulton, S. E.; Wallace, G. G. Bio-ink properties and printability for extrusion printing living cells. *Biomater. Sci.* **2013**, *1* (7), 763–773.
- (47) Duarte Campos, D. F.; Blaeser, A.; Weber, M.; Jäkel, J.; Neuss, S.; Jahnen-Dechent, W.; Fischer, H. Three-dimensional printing of stem cell-laden hydrogels submerged in a hydrophobic high-density fluid. *Biofabrication* **2013**, *5* (1), 015003.
- (48) Shanjani, Y.; Pan, C.; Elomaa, L.; Yang, Y. A novel bioprinting method and system for forming hybrid tissue engineering constructs. *Biofabrication* **2015**, *7* (4), 045008.
- (49) Thakur, T.; Xavier, J. R.; Cross, L.; Jaiswal, M. K.; Mondragon, E.; Kaunas, R.; Gaharwar, A. K. Photocrosslinkable and elastomeric hydrogels for bone regeneration. *J. Biomed. Mater. Res., Part A* **2016**, 104 (4), 879–888.
- (50) Nichol, J. W.; Koshy, S. T.; Bae, H.; Hwang, C. M.; Yamanlar, S.; Khademhosseini, A. Cell-laden microengineered gelatin methacrylate hydrogels. *Biomaterials* **2010**, *31* (21), 5536–5544.
- (51) Cross, L. M.; Thakur, A.; Jalili, N. A.; Detamore, M.; Gaharwar, A. K. Nanoengineered biomaterials for repair and regeneration of orthopedic tissue interfaces. *Acta Biomater.* **2016**, 42, 2–17.
- (52) Yeung, T.; Georges, P. C.; Flanagan, L. A.; Marg, B.; Ortiz, M.; Funaki, M.; Zahir, N.; Ming, W.; Weaver, V.; Janmey, P. A. Effects of

- substrate stiffness on cell morphology, cytoskeletal structure, and adhesion. Cell Motil. Cytoskeleton 2005, 60 (1), 24-34.
- (53) Kaemmerer, E.; Melchels, F. P.; Holzapfel, B. M.; Meckel, T.; Hutmacher, D. W.; Loessner, D. Gelatine methacrylamide-based hydrogels: an alternative three-dimensional cancer cell culture system. *Acta Biomater.* **2014**, *10* (6), 2551–2562.
- (54) Thompson, D. W.; Butterworth, J. T. The nature of laponite and its aqueous dispersions. *J. Colloid Interface Sci.* **1992**, *151* (1), 236–243
- (55) Thakur, A.; Jaiswal, M. K.; Peak, C. W.; Carrow, J. K.; Gentry, J.; Dolatshahi-Pirouz, A.; Gaharwar, A. K. Injectable shear-thinning nanoengineered hydrogels for stem cell delivery. *Nanoscale* **2016**, 8, 12362.